

## Adsorption of terephthalic acid and *p*-toluic acid from aqueous solution using metal organic frameworks: Effect of molecular properties of the adsorbates and structural characteristics of the adsorbents

Alireza Behvandi<sup>a</sup>, Farhad Khorasheh<sup>b,\*</sup>, Ali Akbar Safekordi<sup>a</sup>

<sup>a</sup>Department of Chemical Engineering, Science and Research Branch, Islamic Azad University, Tehran, Iran, email: behvandi.chemeng@gmail.com (A. Behvandi), safekordi@sharif.edu (A.A. Safekordi)

<sup>b</sup>Department of Chemical and Petroleum Engineering, Sharif University of Technology, Tehran, Iran, email: khorashe@sharif.ir (F. Khorasheh)

Received 23 May 2016; Accepted 27 August 2016

### ABSTRACT

The adsorptive removal of terephthalic acid (TPA) and *p*-toluic acid (*p*-tol) by metal organic frameworks (MOF) of Cu-BTC, Fe-BTC, MIL-101(Cr) and MIL-53(Al) was investigated in this study. The influence of various factors including solution pH, contact time, and initial concentration of TPA and *p*-tol solutions on the adsorption behavior was evaluated. Different adsorption isotherms and kinetic models were used to fit experimental adsorption data. It was found that the Langmuir and Redlich-Peterson adsorption isotherms were adequate to represent the experimental data ( $R^2 > 0.97$ ) and that the adsorption kinetics was well-represented by a pseudo-second-order kinetic model ( $R^2 > 0.98$ ). The zeta potential of the four MOFs decreased with increasing pH confirming the importance of the electrostatic interactions between adsorbents and TPA (or *p*-tol) as well as the importance of physicochemical properties of the adsorbates and characteristics of the adsorbents. Highest adsorption capacity for TPA (non-polar) and *p*-tol (polar) were obtained over microporous Cu-BTC (1838.6 mg/g) and mesoporous MIL-53(Al) (1056.7 mg/g), respectively. Furthermore, adsorption studies using an industrial wastewater from a TPA production plant suggested that compared with the conventional adsorbents such as activated carbon and multiwall carbon nanotubes, MOFs (especially mesopore-types) can be used as promising adsorbents in the adsorptive removal of organic pollutants from wastewaters.

**Keywords:** Metal organic framework (MOF); Terephthalic acid; *p*-Toluic acid; Wastewater; Adsorption.

### 1. Introduction

Terephthalic acid (TPA) and para-toluic acid (*p*-tol) are two important cyclic materials that are often present in the waste water streams from industrial plants for production of polyester fibers, PET-films/bottles, drugs, synthetic perfumes, and dyes [1,2]. Purified terephthalic acid, for example, is the main starting material for polyethylene terephthalate (PET) which is used in plastic manu-

facturing. For every ton of TPA produced, about 3 to 4 m<sup>3</sup> of wastewater with 4 to 10 kg COD/m<sup>3</sup> is produced containing mainly *p*-tol, benzoic acid (BA), 4-carboxybenzaldehyde (4-CBA), phthalic acid (PA), and TPA. These five aromatic compounds make up to 75% of the COD (chemical oxygen demand) of these wastewaters that should be removed prior to discharge. The proper treatment of these wastewaters has become very important due to the increased stringent laws on industrial discharge [3,4]. Several methods have been suggested for removal of the TPA or *p*-tol from aqueous systems. Davarpanah

\*Corresponding author.

et al. [2] suggested an anionic exchange resin containing magnetite nanoparticles for removal of *p*-tol from water. Marashi et al. [5] used the bimodal electricity generation of microbial fuel cell for treatment of wastewater containing TPA and *p*-tol. In another investigation, Caliskan et al. [6] reported the adsorption behavior of TPA on TiO<sub>2</sub> nano particles and TiO<sub>2</sub>-SiO<sub>2</sub> composites synthesized by a thermal hydrolysis method. Many other studies have also been conducted focusing on the removal of acidic compounds from aqueous solutions using electro dialysis, solvent extraction, pervaporation, nanofiltration (NF), membranes, and adsorption [3]. Among these methods, adsorption has been found to be most suitable and economic [7]. A review of the literature indicates that the adsorption behavior of acidic compounds on different adsorbents including activated carbons, mesoporous silicas, soils, bentonites, and montmorillonites has been well-documented [8–12]. However, most of these adsorbents either do not have a high enough adsorption capacity, or require a relatively long contact time for adsorption. It is, therefore, of interest to develop effective adsorbents having a higher adsorption capacity or requiring shorter contact times for the removal of organic pollutants from aqueous solution.

Metal organic frameworks (MOFs), also known as coordination polymers, represent a class of novel crystalline adsorbents that have attracted significant attention due to their great diversity in structures resulting from coordination bonds between inorganic metal atoms as nodes and organic ligands as linkers [13–15]. This combination of inorganic metal nodes connected by organic linkers creates a chemically diverse environment inside MOF pores which allows specific interactions between adsorbates and both the organic and the inorganic parts of the framework. The particular interest in MOFs is due to the ease of adjusting their pore size and shape from a micro to a meso scale (by changing the connectivity of the inorganic part and the nature of the organic linkers), thermal and chemical stability, high surface area and functionality [15,16]. These materials can thus be potentially employed for gas storage [17], catalysis [18,19], luminescence [20,21], adsorption/separation [15], and drug delivery [22]. In this study, four well-known water stable MOFs namely Cu-BTC (HKUST-1), Fe-BTC (MIL-100(Fe)), MIL-101(Cr) and MIL-53(Al), which have great potential for aqueous phase adsorption, were prepared by common synthetic routes and, for the first time, were used as adsorbents for adsorption of TPA and *p*-tol from water (HKUST stands for Hong Kong University of Science and Technology and MIL stands for Material of Institut Lavoisier). Adsorption experiments were performed to systematically investigate the effects of solution pH on the adsorption behavior as well as quantitative modeling of equilibrium adsorption isotherms and adsorption kinetics. Zeta potential, TEM, BET and XRD analyses were used for characterization of adsorbents. The adsorption performance of MOFs was compared with other adsorbents including activated carbon (AC) and multi-wall carbon nanotubes (MWCNT) using an industrial wastewater. Results indicated the promising potential of MOFs as adsorbents for wastewater treatment compared with other conventional adsorbents.

## 2. Experimental

### 2.1. Material and reagents

All solvents and reagents were purchased from Merck and were used without further purification. Copper (II) nitrate trihydrate [Cu(NO<sub>3</sub>)<sub>2</sub>·3H<sub>2</sub>O, 0.98%], 1,3,5-benzene tricarboxylic acid (H<sub>3</sub>BTC, 95%) and ethanol (dried, 99.98%) were used in Cu-BTC synthesis. Chromium (III) nitrate nonahydrate [Cr(NO<sub>3</sub>)<sub>3</sub>·9H<sub>2</sub>O, 98%], terephthalic acid (TPA, 98%) and hydrofluoric acid (HF, 40%) were used to synthesize MIL-101(Cr). Nitric acid (65%), hydrofluoric acid (HF, 40%), iron (III) nitrate nonahydrate [Fe(NO<sub>3</sub>)<sub>3</sub>·9H<sub>2</sub>O, 98%], and H<sub>3</sub>BTC were used to prepare Fe-BTC. Aluminum (III) nitrate nonahydrate [Al(NO<sub>3</sub>)<sub>3</sub>·9H<sub>2</sub>O, 98%], HF, and TPA were used to synthesize MIL-53(Al). Ethanol (dried, 99.98%) and N,N-dimethylformamide (DMF, 99%) that were used for purification of the synthesized MOFs, and *p*-toluic acid (*p*-tol, 99%) were also obtained from Merck.

#### 2.1.1. Synthesis of Cu-BTC (HKUST-1)

The method used for synthesis of Cu-BTC was based on the work of Wang and co-workers [23]. Briefly, 1.996 g of Benzene-1,3,5-tricarboxylic acid (9 mmol) was added to ethanol (20 ml) and mixed thoroughly until it was completely dissolved. 4.48 g of cupric nitrate trihydrate (18 mmol) was dissolved into deionized water (10 ml) in another flask. The two solutions were then mixed and stirred at room temperature for 16 h. The mixture was then transferred into a 50 ml teflon-lined stainless steel autoclave, sealed, and subsequently heated to 140°C for 48 h. The reaction vessel was then allowed to cool to room temperature. Blue crystals of Cu-BTC were recovered by filtration with Buchner funnel (soft filter paper 2–3 μm) and washed thoroughly with deionized water. This product was dried at 85°C under vacuum overnight.

#### 2.1.2. Synthesis of Fe-BTC (MIL-100(Fe))

According to the method proposed by Yoon and co-workers [24], iron powder (0.28 g), H<sub>3</sub>BTC (0.69 g), hydrofluoric acid (0.2 ml), and nitric acid (0.19 ml) were well mixed with ultrapure water (20 ml) and placed in a 50 ml teflon-lined stainless steel autoclave. The autoclave was then placed in an oven at 150°C for 12 h. After allowing it to cool to room temperature, the light orange solid product was collected by filtration and washed with ultrapure water. The as-synthesized Fe-BTC was further purified with hot water at 80°C for 5 h to remove residual unreacted ions, and then with hot ethanol at 60°C for 3 h until no colored impurities was detected in the mother liquor solution. The purified Fe-BTC was then collected by a soft filter paper (2–3 μm) and the solid was subsequently dried at 85°C under vacuum overnight.

#### 2.1.3. Synthesis of MIL-101(Cr)

MIL-101(Cr) was synthesized according to the method described in the literature [25,26] where 2 g of chromium nitrate (5 mmol), 0.83 g of TPA (5 mmol), 0.25 ml HF, and 25 ml ultrapure water were well mixed for 30 min followed

by ultra-sonication for 15 min. The mixture was then transferred into a 50 ml Teflon-lined stainless steel autoclave, sealed, heated to 220°C for 8 h, and subsequently cooled to room temperature. The green suspension of MIL-101 was then filtered using Buchner funnel with a glass filter to remove the re-crystallized needle-shaped colorless TPA which remained on the filter and the MIL-101 suspension which passed through it. The suspension was again filtered by soft filter paper (2–3  $\mu\text{m}$ ) to recover the green-colored products. To remove the unreacted TPA, the as-synthesized MIL-101 was further washed (twice) by 30 ml DMF at 70°C for 8 h with continuous stirring. After filtration, the synthesized MIL-101 was washed (twice) by 30 ml dried ethanol for 8 h to remove the DMF and additional water and was subsequently filtered again. The purified MIL-101 was dried overnight at 150°C and stored in a desiccator after cooling to room temperature.

#### 2.1.4. Synthesis of MIL-53(Al)

According to a solvothermal method reported in the literature [27,28], aluminum nitrate (6.5 g), TPA (1.44 g), and ultrapure water (25 ml) were well mixed for 30 min followed by ultra-sonication for 15 min. The mixture was then transferred into a 50 ml teflon-lined stainless steel autoclave, sealed, heated up to 220°C for 72 h. After the completion of reaction, the autoclave was allowed to cool to room temperature. The white powder formed was then filtered and subsequently washed with ultrapure water until pH of filtrate was  $\sim 7$ . To remove the unreacted TPA, the as-synthesized MIL-53(Al) was further washed (twice) by 30 ml DMF at 70°C for 8 h with continuous stirring. After filtration, it was washed (twice) by 30 ml dried ethanol for 8 h, filtered, and dried at 85°C under vacuum overnight.

#### 2.2. Characterizations

A dynamic back light scattering technique (Malvern ZS Nano series) was used to measure the zeta potential of the particles. The  $p\zeta$ -pH curves were produced using the MPT-2 Autotitrator in conjunction with the Malvern Zetasizer Nano. The autotitrator was connected to a sulphide resistant pH probe which was inserted into the sample measurement cell. Sample pH adjustment was achieved by the addition of either 0.1M HCl or 0.05 M NaOH. Powder XRD pattern was obtained in an XPert pro diffractometer (Panalytical Corp., Netherlands) using  $\text{CuK}\alpha$  radiation and a wavelength of 1.79 Å to determine the crystalline phases of the MOFs and to obtain the average crystallite size using Scherer's equation. The voltage and anode current were 40 kV and 30 mA, respectively, and the scanning range was  $2\theta = 1\text{--}100^\circ$  with a step size of  $0.01^\circ$ . The nitrogen adsorption-desorption isotherm, Langmuir and Brunauer–Emmett–Teller (BET) surface areas and pore volumes of all adsorbents were measured on a Micromeritics ASAP 2010 sorptometer using  $\text{N}_2$  adsorption at 77 K. For these measurements, the powder was degassed and activated under vacuum at 105°C for 3 h. The crystalline structure of MOFs was identified by a transmission electron microscope (TEM) images taken at 80 kV by a JEM1230 instrument (JEOL Corp., Japan).

#### 2.3. Adsorption experiments

The solutions of TPA and *p*-tol with desired concentrations were prepared using deionized water. The TPA or *p*-tol concentrations before and after the adsorption experiment were determined by high-performance liquid chromatography (HPLC) using a Waters model 600E instrument (USA) equipped with a 150 mm long C18 column and a UV detector with wavelength set at 230 nm. The mobile phase consisted of 21% (by volume) acetonitrile, 0.1% trifluoroacetic acid, and 78.9% HPLC-grade water. Before adsorption, the adsorbents were dried overnight under vacuum at 100°C, and an exact amount of the adsorbents (7.0 mg) was placed in the aqueous solution (20 ml) with desired concentration (in the range of 100 to 3000 mg/l). The solutions containing the adsorbent were kept well-mixed using magnetic stirring for a specified period of time (15 min to 24 h) at a constant temperature (25°C). After the specified adsorption time, the solution was separated from the adsorbents using a slow flow cellulose filter paper (2–3  $\mu\text{m}$ ). To determine the adsorption capacity at various pH values, the pH value of the solutions was adjusted with addition of 0.05 M NaOH or 0.1 M HCl aqueous solutions. The equilibrium parameters for TPA and *p*-tol adsorption over the four synthesized MOFs were determined using different adsorption isotherms including Langmuir, Freundlich, and Redlich–Peterson models using data from experiments with adsorption time of 24 h for different initial concentration of adsorbates. The kinetic constants for pseudo-first-order and pseudo-second-order kinetic models were obtained using adsorption data at different adsorption times. The amount of TPA or *p*-tol adsorbed on the adsorbents was calculated by mass balance Eq. (1):

$$q_t = (C_0 - C_t) \frac{V}{W} \quad (1)$$

where  $q_t$  (mg/g) is the amount of adsorbate adsorbed at time  $t$  (min),  $C_0$  and  $C_t$  (mg/l) are the liquid-phase concentrations of TPA or *p*-tol at time = 0 and  $t$ , respectively, and  $V$  (l) and  $W$  (g) are the volume of the solution and the mass of the adsorbent, respectively.

### 3. Results and discussion

#### 3.1. Characterization results

Powder XRD patterns of Cu-BTC, Fe-BTC, MIL-101(Cr) and MIL-53(Al) are shown in Fig. 1a. The main diffraction peaks matched the XRD patterns reported by other investigators [16,29–34]. The high intensities of the diffraction peaks between 2.5 to 20 degrees for all MOFs indicated a good crystallinity of all synthesized materials. The FT-IR spectra of the four MOFs as shown in Fig. 1b are similar to those reported by other investigation [35–39]. The bands near  $3400\text{ cm}^{-1}$  can be assigned to O–H and the strong bands at  $1540$  and  $1400\text{ cm}^{-1}$  can be assigned to the vibrational stretching frequencies of the framework (O–C–O) confirming the presence of carboxylate linker in the frameworks. The strong peaks ascribed to C=O stretching vibration at  $1710\text{--}1720\text{ cm}^{-1}$  (for Fe-BTC and Cu-BTC) and  $1690$  (for MIL-101 and MIL-53) in the samples, are assigned to

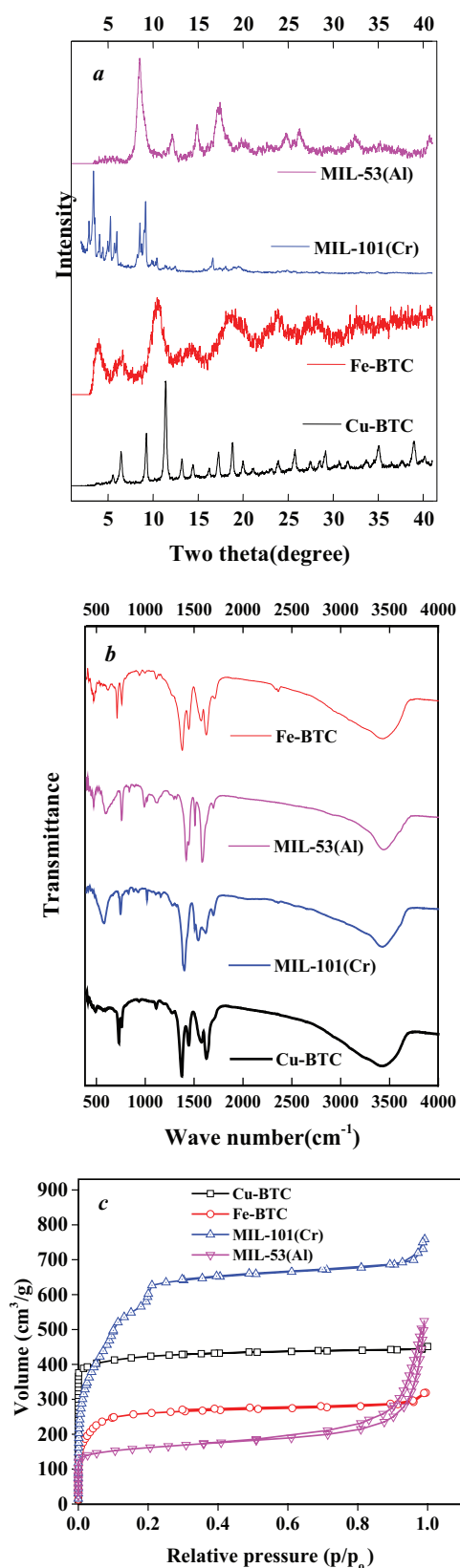


Fig. 1. (a) XRD patterns, (b) FT-IR spectra and (c) N<sub>2</sub> adsorption isotherms at 77 K of synthesized MOFs.

residual trimesic acid and terephthalic acid, respectively. The bands near 1020 and 750 cm<sup>-1</sup> can be assigned to the vibrations of benzene rings. The bands near 570 cm<sup>-1</sup> are most likely ascribed to in-plane and out-of-plane bending modes of COO<sup>-</sup> groups. The nitrogen adsorption-desorption isotherms of the dehydrated MOFs are shown in Fig. 1c indicating a typical type-I uptake profile for Cu-BTC, Fe-BTC, and MIL-101(Cr) (micropore volume is dominant) and type-4 profile for MIL-53(Al) (mesopore volume is dominant). The TEM images shown in Fig. 2 confirmed that the synthesized MOFs were highly crystallized with regular topologies and were similar to those reported by other investigators [32,38,40–44]. The BET surface area, average pore diameter, and pore volume of the MOFs measured by N<sub>2</sub> adsorption at 77 K and presented in Table 1, are in good agreement with reported values in most previous investigations [36,41,45,46]. The slight differences compared with results reported by other similar investigations could be related to the differences in the synthesis and purification methods. As shown in Table 1, the average pore diameter of MOFs increased in the following order Cu-BTC < Fe-BTC

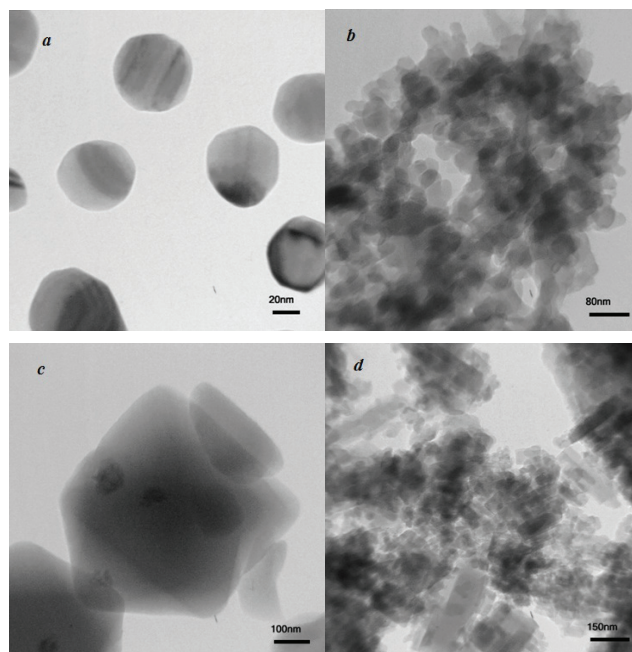


Fig. 2. TEM images of (a) Cu-BTC, (b) Fe-BTC, (c) MIL-101(Cr), and (d) MIL-53(Al).

Table 1  
Pore volumes, average pore diameters, and surface areas for different adsorbents

Sample	S <sub>BET</sub> (m <sup>2</sup> /g)	Avg. pore diameter (nm)	V <sub>micro</sub> (m <sup>3</sup> /g)	V <sub>total</sub> (m <sup>3</sup> /g)	V <sub>micro</sub> /V <sub>total</sub>
Cu-BTC	1601	1.73	0.65	0.69	0.94
Fe-BTC	1031	1.89	0.40	0.49	0.82
MIL-101(Cr)	2390	2.23	0.98	1.32	0.74
MIL-53(Al)	598.2	5.41	0.25	0.81	0.31

< MIL-101(Cr) < MIL-53(Al) and the ratio of micropore volume to total volume decreased in the following order Cu-BTC > Fe-BTC > MIL-101(Cr) > MIL-53(Al) in agreement with N<sub>2</sub> adsorption-desorption isotherms of Fig. 1c.

### 3.2. Adsorption studies

#### 3.2.1. Adsorption isotherms

The adsorption performance of the synthesized MOFs for the removal of TPA and *p*-tol from the aqueous phase was compared with two other common adsorbents including activated carbon (AC) and multiwall carbon nanotubes (MWCNT). The equilibrium adsorption capacities for each adsorbent are presented in Fig. 3 for initial adsorbate concentration of 2000 mg/l indicating the superior performance of the MOFs. Adsorption experiments were then performed to obtain the equilibrium adsorption isotherms for each MOF. The Langmuir adsorption isotherm was used to evaluate the adsorption behavior of TPA and *p*-tol on different adsorbents. This isotherm is often successfully applied for adsorption of many organic pollutants from aqueous solutions [47]. The Langmuir isotherm assumes physical (monolayer) adsorption onto a surface which consists of a finite number of active sites having a uniform energy [48]. The linear form of the Langmuir isotherm is given by:

$$\frac{C_e}{q_e} = \frac{C_e}{q_o} + \frac{1}{q_o K_L} \quad (2)$$

where  $C_e$  (mg/l) is the equilibrium concentration of adsorbate,  $q_e$  (mg/g) is the amount of adsorbate adsorbed at equilibrium,  $q_o$  (mg/g) is the maximum adsorption capacity, and  $K_L$  (l/mg) is the Langmuir constant that is related to the free energy of adsorption. Adsorption isotherms for TPA and *p*-tol uptake on each MOF were obtained after a relatively long adsorption time (24 h) and the results are presented in Fig. 4. The values of  $K_L$  and  $q_o$  were calculated from the slope and intercept of linear plots of  $(C_e/q_e)$  against  $C_e$  and are reported in Table 2 indicating that all MOFs have high

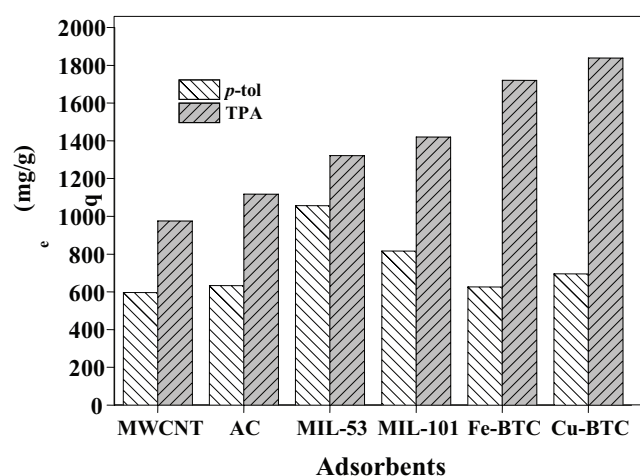


Fig. 3. Equilibrium adsorption capacity ( $q_e$ ) of TPA and *p*-tol over different adsorbents ( $C_o = 2000$  mg/l,  $T = 25^\circ\text{C}$ ,  $t = 24$  h).

adsorption capacity for TPA and *p*-tol and that the adsorption capacity for TPA was higher than that for *p*-tol for all MOFs. In addition to the surface and pore characteristics of porous adsorbents, the difference in physical or chemical properties of the adsorbates such as the size and shape of molecule, surface area, surface tension, polarizability, ionization potential, heat of vaporization and electron affinity, play important roles in their adsorption behavior on the adsorbents [38,49]. The molecular properties of TPA and *p*-tol are presented in Table 3.

Prior to the interaction of the benzene rings of TPA and *p*-tol with the active sites, the adsorbate molecules should enter the pores of MOFs [50]. The diameter of the maximum plane of TPA and *p*-tol depends on the distance between the two carboxyl groups for TPA and between methyl and carboxyl groups for *p*-tol (linking benzene ring with an angle of about  $180^\circ$ ). The adsorbate molecules can enter into adsorbent pores having diameters larger than the maximum plane of guest molecules [38]. The adsorption capacity for the adsorbates filling the pores of MOFs would depend on the length of the diagonal line of the molecular rectangle plane. The adsorbent-adsorbate interactions is also affected by the average diameter of adsorbents pores [51,52]. When the average pore diameter is small or the guest molecule is large enough, the distance between the organic molecule and the internal surface of adsorbents is reduced and their interaction potential is increased [49,53]. Hence, a smaller diameter of pores would induce a higher heat of adsorption ( $-\Delta H_{\text{ads}}$ ) and more adsorption capacity for TPA compared with *p*-tol. As indicated in Table 3, although the dipole moment of TPA is zero (TPA is a non-polar component), its polar surface area, polarizability, electron affinity, radius of gyration and molecular rectangle plane (the length of diagonal line of molecule) is higher than *p*-tol indicating that TPA has a better chance to be trapped into the pores of MOFs especially in the micropores. The hydrogen bonding between the hydrogen in carboxyl groups of TPA and the oxygen in the adsorbent structure is stronger than those for *p*-tol due to the existence of two carboxyl groups in TPA [54,55]. The same observations were also reported in liquid phase adsorption [56] and in gas phase adsorption [57] as adsorption capacities or adsorption energies were correlated with the molecular connectivity index emphasizing the main influence of the molecular topology or shape, i.e., branching and size. Giraudet and co-workers [49] pointed to the effect of polarizability, heat of vaporization, ionization potential, and surface tension of adsorbates and the average micropore radius for adsorbents on the heats of adsorption. They concluded that the heat of adsorption must be more dependent on the properties of adsorbates than on the physical characteristics of adsorbents [49].

It can be seen from Fig. 4a that the uptake of TPA on the MOF adsorbents is in the order of Cu-BTC > Fe-BTC > MIL-101(Cr) > MIL-53(Al). According to Table 1, although the specific surface area of MIL-101(Cr) is greater than other MOFs, it was not the dominant adsorbent for TPA uptake. Cu-BTC (which has the smallest average pore diameter) has the highest adsorption capacity for TPA. The average pore diameter of the four MOFs is in the order Cu-BTC < Fe-BTC < MIL-101(Cr) < MIL-53(Al) and the ratio of their micropore volume to total pore volume is in reverse order confirming that the pore diameter of adsorbents is an important factor

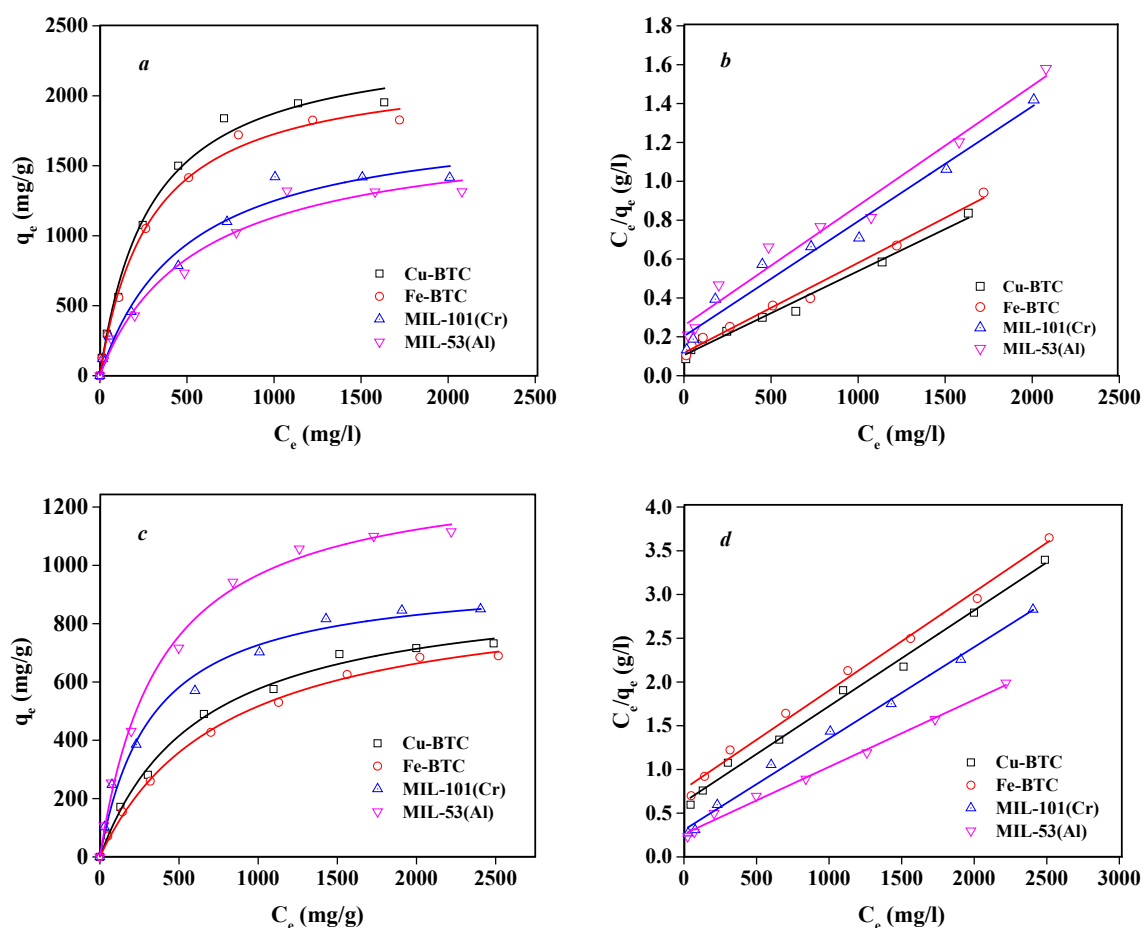


Fig. 4. Adsorption isotherms and Langmuir plots for TPA (a, b) and *p*-tol (c, d) for different adsorbents at  $T = 25^{\circ}\text{C}$ .

Table 2

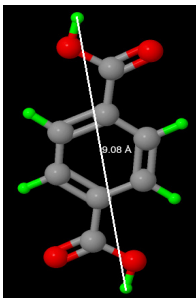
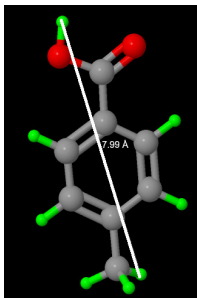
Equilibrium parameters for TPA and *p*-tol adsorption over different adsorbents at  $T = 25^{\circ}\text{C}$

Adsorbate	Adsorbents	Langmuir model			Freundlich model			Redlich–Peterson model			
		$q_0$ (mg/g)	$K_L$ (l/mg)	$R^2$	$K_F$ (mg/g(l/mg) <sup>1/n</sup> )	$1/n$	$R^2$	$a_R$ (l/mg) <sup>-β</sup>	$K_R$ (l/g)	$\beta$	$R^2$
TPA	Cu-BTC	2312.4	$4.10 \times 10^{-3}$	0.99	36.05	0.583	0.96	$3.45 \times 10^{-3}$	8.33	1	0.99
	Fe-BTC	2159.5	$3.94 \times 10^{-3}$	0.99	33.44	0.579	0.96	$3.43 \times 10^{-3}$	7.65	1	1.00
	MIL-101(Cr)	1692.0	$2.91 \times 10^{-3}$	0.97	33.11	0.529	0.95	$2.03 \times 10^{-3}$	3.78	1	0.97
	MIL-53(Al)	1620.8	$2.39 \times 10^{-3}$	0.97	21.87	0.564	0.95	$1.81 \times 10^{-3}$	3.19	1	0.97
<i>p</i> -tol	Cu-BTC	909.1	$1.75 \times 10^{-3}$	0.99	10.04	0.572	0.97	$1.59 \times 10^{-3}$	1.49	1	1.00
	Fe-BTC	885.0	$1.46 \times 10^{-3}$	0.99	8.07	0.588	0.98	$2.30 \times 10^{-3}$	1.27	1	1.00
	MIL-101(Cr)	952.4	$3.40 \times 10^{-3}$	0.99	28.47	0.457	0.96	$24.7 \times 10^{-3}$	5.30	0.937	0.99
	MIL-53(Al)	1302.4	$2.93 \times 10^{-3}$	0.99	24.00	0.525	0.97	$2.42 \times 10^{-3}$	3.33	0.809	0.99

for adsorption of TPA [49,51]. The results indicate that the adsorbent having higher micropore volume and smaller pore size is the superior candidate for adsorption of TPA. The uptake of *p*-tol over MOFs under similar conditions used for TPA adsorption was in the order of MIL-53(Al) > MIL-101(Cr) > Cu-BTC > Fe-BTC (Fig. 4c). This observation can be explained in terms of the capillary forces for high coverage of the adsorbent surface related to the surface

tension, contact angle, and solid surface roughness and geometry [49,58]. In micropores, the intermolecular attractive forces between the adsorbate and the adsorbent molecules are likely to predominate [59]. In mesopores (pores with widths equal several times the diameter of adsorbate molecules), however, the capillary forces are predominant [58]. The capillary effect in porous media results from two opposing forces; liquid adhesion to solid surfaces that

Table 3  
Physico-chemical characteristics of TPA and *p*-tol

Item	TPA	<i>p</i> -tol	Unit
Molecular structure			–
Molecular weight	166.13	136.15	g/mole
Polarizability	15.97	14.99	Å <sup>3</sup>
Ionization potential	226.3	211.4	kcal/mole
Electron affinity	43.47	15.64	kcal/mole
Surface tension (at 25°C)	77.3	52.9	mN/m
Standard state absolute entropy	62.30	66.93	cal/mole·K
Heat of vaporization (at 25°C)	34.81	22.43	kcal/mole
Topological polar surface area	74.6	37.3	Å <sup>2</sup>
Radius of Gyration	4.85	4.33	Å
pKa	3.51–4.82	4.36	–
Dipole moment	0	2.32	debye
Maximum distance between H atoms (molecular rectangle plane)	9.08	7.99	Å

tends to spread the liquid, and the cohesive surface tension force of liquids that acts to reduce the interfacial area [60]. As indicated in Table 3, the surface tension of *p*-tol is lower than TPA confirming the fact that the capillary effect (that is predominant in mesoporous solids) is an important parameter for adsorption of the polar *p*-tol molecules making MIL-53(Al) the superior adsorbent for *p*-tol. It is worth noting that the 3D framework structure of MIL-53(Al) could adjust the shape and size of the porous channels when it absorbs some polar and hydrocarbon molecules. This adjustment that is called the “breathing” effect of framework [37] may have a special effect on adsorptive behavior of MIL-53(Al), but was not considered in our analysis. For other three MOFs, the surface area of adsorbents is in the order of MIL-101 > Cu-BTC > Fe-BTC that is the same order for uptake of *p*-tol on them, confirming the effect of surface area on adsorption capacity of polar *p*-tol on adsorbents having higher micropore volume [61,62]. In addition, the chemical nature of the adsorbent surface which is influenced by solution pH, plays an important role in the adsorption of adsorbates from aqueous solutions [63,64]. In order to confirm this, the zeta potential of the four MOFs in solutions with different pH values was determined (Fig. 5). The zeta potential decreased with increasing pH, suggesting that the electrostatic interaction between positively charged adsorbents and negative adsorbates in the adsorption process [55]. As shown in Fig. 5, at lower pH values, zeta potential of adsorbents is in the order of MIL-53(Al) > MIL-101 > Cu-BTC > Fe-BTC. It seems that due to the polarity of *p*-tol, the interaction between dipole of solute and the

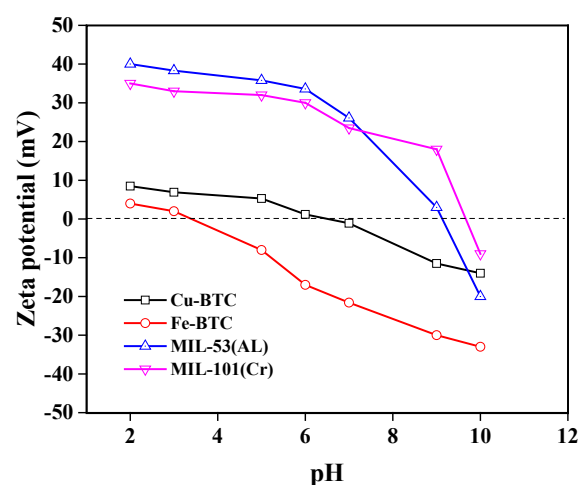


Fig. 5. Zeta potential of adsorbents at different pH values.

partial positive charges in adsorbents is more favored [49] making the electrostatic interaction an important factor for adsorption of polar molecules like *p*-tol.

Equilibrium adsorption data for TPA and *p*-tol adsorption were fitted by Langmuir and Freundlich adsorption isotherms. The Freundlich adsorption isotherm is a special case for heterogeneous surface energy in which the energy term in the Langmuir equation varies as a function of surface coverage and is not restricted to monolayer formation.

This model is an empirical approach for adsorbents with very uneven adsorbing surfaces [47,65]. The Freundlich adsorption isotherm is given by:

$$q_e = K_F C_e^{\frac{1}{n}} \quad (3)$$

where  $C_e$  (mg/l) is equilibrium concentration of adsorbate,  $q_e$  (mg/g) is the amount of adsorbate adsorbed at equilibrium, and  $K_F$  (mg/g(l/mg)<sup>1/n</sup>) and  $1/n$  represent the Freundlich constants corresponding to the adsorption capacity and adsorption intensity, respectively.  $K_F$  and  $1/n$  were determined from the intercept and slope of the linear plots of  $\ln(q_e)$  against  $\ln(C_e)$  for the four adsorbents and are reported in Table 2. The linear form of the Freundlich equation is given by:

$$\ln q_e = \ln K_F + \left(\frac{1}{n}\right) \ln C_e \quad (4)$$

The magnitude of the exponent  $1/n$  gives an indication of the favorability of adsorption. Values of  $n > 1$  represent favorable adsorption conditions [66]. The results presented in Table 2 indicate that the linear correlation coefficients ( $R^2$ ) for the Langmuir adsorption isotherm were slightly higher than those for the Freundlich isotherm. It seems that the monolayer adsorption is more favorable for adsorption of both TPA and *p*-tol over all four adsorbents. However, due to proximity of correlation coefficients for the two models, a third adsorption isotherm (Redlich-Peterson (R-P)) was used to confirm the obtained results. The Redlich-Peterson isotherm amends the inaccuracies of two parameter Langmuir and Freundlich isotherms in most adsorption systems. This model is a hybrid isotherm featuring both Langmuir and Freundlich isotherms which incorporates three parameters into an empirical equation as follows [47,67]:

$$q_e = \frac{K_R C_e}{1 + a_R C_e^\beta} \quad (5)$$

where  $K_R$  (l/g) and  $a_R$  (1/mg)  $\beta$  are the Redlich-Peterson isotherm constants and  $\beta$  is R-P isotherm exponent. The model has a linear dependence on concentration in the numerator and an exponential function in the denominator to represent adsorption equilibria over a wide concentration range, that can be applied either in homogeneous or heterogeneous systems due to its versatility [68]. Typically, a minimization procedure is adopted in solving the equation by maximizing the correlation coefficient between the experimental data points and theoretical model predictions. In the limit, it approaches the Freundlich isotherm model at high concentrations (as the exponent  $\beta$  tends to zero) and is in accordance with the low concentration limit of the ideal Langmuir model (as the  $\beta$  values are all close to one) [47,68]. The results obtained from R-P equation are also presented in Table 2. By comparing the values of  $R^2$ , the Langmuir isotherm gave a better fit of the adsorption data compared with the Freundlich isotherm. However, the Redlich-Peterson model showed an improved fit for both TPA and *p*-tol. As shown in Table 2, the exponent  $\beta$  of the R-P model for TPA and *p*-tol over four MOFs was obtained as 1 by the minimization algorithm (with the exception for adsorption of *p*-tol over MIL-101(Cr) and MIL-53(Al)) con-

firmed that the Langmuir isotherm (monolayer adsorption mechanism) is more adequate. The slightly lower values for  $\beta$  for adsorption of *p*-tol over MIL-101(Cr) and MIL-53(Al) might be related to the more mesoporous structure of these adsorbents resulting in the dominance of capillary forces and multilayer adsorption especially in later stage of the adsorption process [69].

### 3.2.2. Adsorption kinetics

Dynamic adsorption data for TPA and *p*-tol over the four MOFs are presented in Fig. 6. The adsorption process was rapid at the beginning of each adsorption experiment due to the abundant presence of vacant surface sites. As time passed, the number of vacant sites decreased as the adsorption sites became saturated and ultimately equilibrium was achieved [70,71]. For all adsorbents, most of the TPA and *p*-tol were adsorbed during the first 4 h from the start of each adsorption experiment. The adsorption time was extended to 24 h to achieve equilibrium. To describe the kinetics of adsorptions, the dynamic adsorption data were treated with pseudo-first order and pseudo-second order kinetic models [33,72]. The pseudo-first order model is expressed by the following equations:

$$\frac{dq_t}{dt} = k_1 (q_e - q_t) \quad (6)$$

$$\ln(q_e - q_t) = \ln \ln q_e - k_1 t \quad (7)$$

where  $q_t$  and  $q_e$  are the adsorbed amount of TPA or *p*-tol (mg/g) at time  $t$  (min) and at equilibrium, respectively.  $k_1$  is the pseudo-first order kinetic constant (1/min). Eq. (7) is derived from Eq. (6) by integrating subject to the initial condition. The pseudo-first order kinetics has been utilized for a variety of adsorption processes especially in water treatment [45,73]. The equilibrium adsorption capacity ( $q_e$ ) and kinetic constant ( $k_1$ ) were calculated from the intercept and slope of linear plots of  $\ln(q_e - q_t)$  against  $t$  and are reported in Table 4. Dynamics of TPA and *p*-tol adsorption can also be interpreted by pseudo-second order kinetics that is expressed by the following equations [72,73]:

$$\frac{dq_t}{dt} = k_2 (q_e - q_t)^2 \quad (8)$$

$$\frac{t}{q_t} = \frac{1}{k_2 q_e^2} + \frac{1}{q_e} t \quad (9)$$

where  $k_2$  (g/mg·min) is the pseudo-second order rate constant. Eq. (9) was derived from Eq. (8) by integrating subject to the initial condition. Fig. 6 shows the linear plots of  $t/q_t$  against  $t$  for pseudo-second order kinetic analysis of TPA and *p*-tol adsorption on different adsorbents for different initial concentrations.  $k_2$  and  $q_e$  were calculated from the intercepts and slopes of these plots and are reported in Table 4. Comparison of the correlation coefficients ( $R^2$ ) reported in Table 4 indicates that the adsorption kinetics is more adequately represented by a pseudo-second order rather than a pseudo-first order model. Furthermore, the values for maximum adsorption capacity ( $q_e$ ) calculated



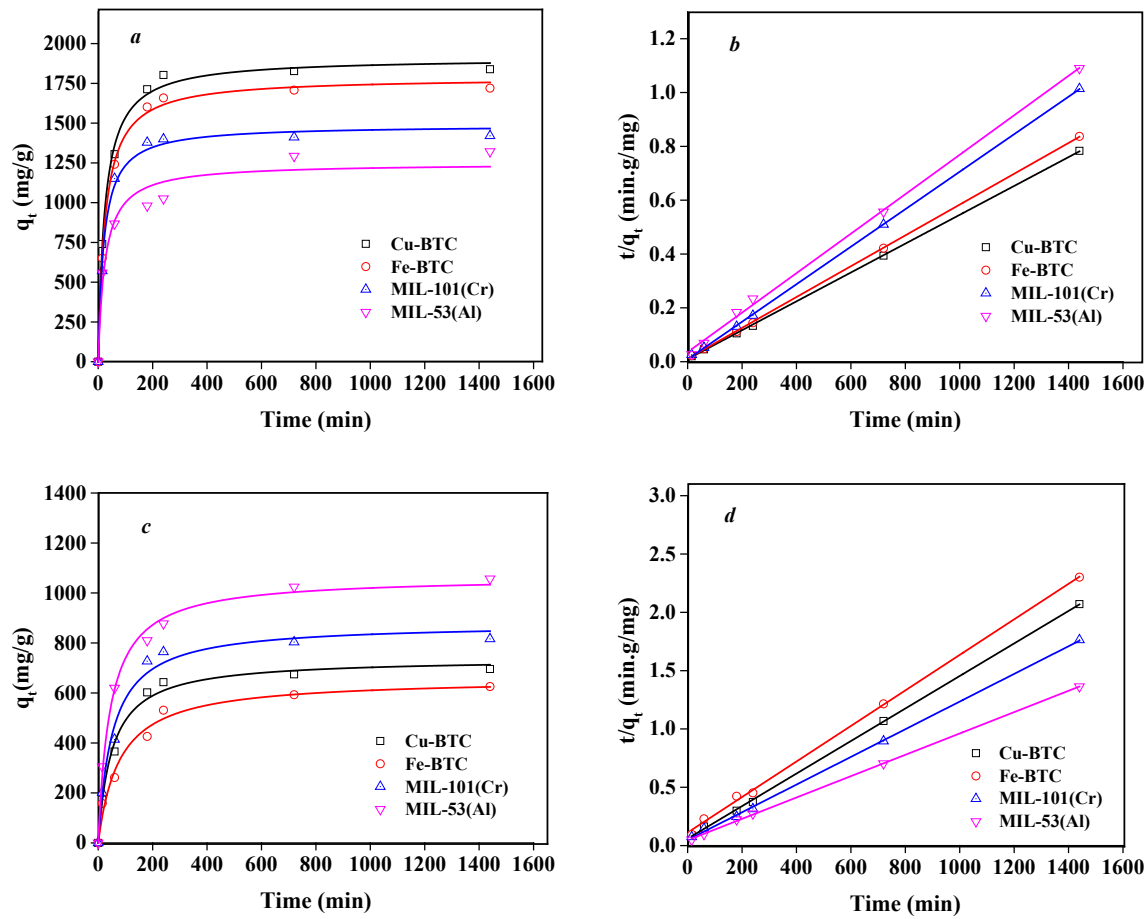


Fig. 6. Dynamic adsorption data for TPA (a) and *p*-tol (c) and pseudo-second order plots of TPA (b) and *p*-tol (d) adsorption over the different adsorbents at initial concentration of  $C_0=2000$  mg/l and  $T = 25^\circ\text{C}$ .

Table 4  
Kinetic parameters for TPA and *p*-tol adsorption on different MOFs at various initial concentrations

Adsorbate	$C_0$ (mg/l)	Adsorbents	Pseudo-first order kinetics			Pseudo-second order kinetics			$q_{e,exp}$ (mg/g)
			$q_{e,cal}$ (mg/g)	$k_1$ ( $\text{min}^{-1}$ )	$R^2$	$q_{e,cal}$ (mg/g)	$k_2$ (g/(mg min))	$R^2$	
TPA	1000	Cu-BTC	430.4	$5.80 \times 10^{-3}$	0.69	1093.6	$4.57 \times 10^{-5}$	0.99	1077.2
		Fe-BTC	473.3	$5.41 \times 10^{-3}$	0.77	1069.3	$4.02 \times 10^{-5}$	0.99	1051.4
		MIL-101(Cr)	301.4	$4.90 \times 10^{-3}$	0.67	793.7	$6.62 \times 10^{-5}$	0.99	785.7
		MIL-53(Al)	469.4	$4.16 \times 10^{-3}$	0.94	757.6	$2.60 \times 10^{-5}$	0.98	734.3
	2000	Cu-BTC	754.1	$6.67 \times 10^{-3}$	0.76	1865.9	$2.93 \times 10^{-5}$	0.99	1838.6
		Fe-BTC	755.9	$6.35 \times 10^{-3}$	0.81	1746.8	$2.91 \times 10^{-5}$	0.99	1720.0
		MIL-101(Cr)	431.0	$6.51 \times 10^{-3}$	0.64	1435.1	$5.35 \times 10^{-5}$	0.99	1420.1
		MIL-53(Al)	874.6	$4.79 \times 10^{-3}$	0.95	1363.8	$1.51 \times 10^{-5}$	0.98	1321.4
<i>p</i> -tol	1000	Cu-BTC	283.2	$4.93 \times 10^{-3}$	0.82	505.1	$4.74 \times 10^{-5}$	0.99	490
		Fe-BTC	300.5	$3.70 \times 10^{-3}$	0.87	448.4	$3.00 \times 10^{-5}$	0.98	427.1
		MIL-101(Cr)	304.6	$5.44 \times 10^{-3}$	0.77	588.2	$4.48 \times 10^{-5}$	0.98	570
		MIL-53(Al)	445.8	$3.90 \times 10^{-3}$	0.88	740.7	$2.68 \times 10^{-5}$	0.99	716.6
	2000	Cu-BTC	388.9	$4.62 \times 10^{-3}$	0.76	719.4	$3.24 \times 10^{-5}$	0.99	695.7
		Fe-BTC	445.1	$3.92 \times 10^{-3}$	0.89	657.9	$2.07 \times 10^{-5}$	0.98	625.7
		MIL-101(Cr)	469.6	$5.59 \times 10^{-3}$	0.83	840.3	$2.92 \times 10^{-5}$	0.98	816.3
		MIL-53(Al)	700.1	$4.50 \times 10^{-3}$	0.94	1092.8	$1.81 \times 10^{-5}$	0.99	1056.7

from the pseudo-second order model were in better agreement with the experimental values.

The dynamic adsorption data can be used to identify the rate-controlling step in the adsorption process. Transport of the adsorbate to the external surface of the adsorbent (film diffusion), transport of the adsorbate into the pores of the adsorbent (intraparticle diffusion) and the adsorption of the adsorbate on the surface of the adsorbent are three consecutive steps involved in the adsorption of an adsorbate by a porous material. As long as the last step is fast enough, the slowest transport portion would determine the overall rate of adsorption [74]. The intraparticle diffusion model based on the theory proposed by Weber and Morris [75,76] would lead to the following equation:

$$q_t = k_d t^{0.5} + F \quad (10)$$

where  $q_t$  (mg/g) is the amount adsorbed at time  $t$ ,  $k_d$  (mg/g·min<sup>1/2</sup>) is the intraparticle diffusion rate constant, and  $F$  (mg/g) is a constant related to the thickness of the boundary layer. If the value of  $F$  is zero, that is, the diffusion model plot of  $q_t$  against  $t^{0.5}$  exhibits a straight line going through the origin, the adsorption process is only controlled by the intraparticle diffusion [74]. However, if the data exhibit multi-linear plot, then two or more steps influence the sorption process. The first sharper portion is the surface adsorption or instantaneous adsorption stage. The second portion is the gradual adsorption stage where intraparticle diffusion limits the rate of adsorption [77]. The diffusion model plots for TPA and *p*-tol adsorption over different adsorbents shown in Fig. 7 suggests a two-stage adsorption process; surface adsorption and intraparticle diffusion. The first linear portion of the plot is due to surface adsorption (faster step) while the second linear portion is due to the intraparticle diffusion within the pores of MOFs (slower step) [77,78]. According to the results reported in Table 5, the values of the slope of slower portion ( $k_d$ ) are not zero, which confirms that intraparticle diffusion controls the adsorption rate at the beginning. Furthermore, the intercept value ( $F$ ) increased with increasing initial concentration of

adsorbates suggesting that intraparticle diffusion is not the only rate-limiting step and that film diffusion also plays an important role in the adsorption of TPA and *p*-tol onto the four MOFs [78].

To determine the mode of diffusion, the following equation can be used for the analysis of dynamic adsorption data [75]:

$$\ln \ln \left( \frac{q_t}{q_e} \right) = \ln \ln k_m + m \ln t \quad (11)$$

where  $k_m$  is the adsorbent–adsorbate interaction coefficient and  $m$  is a transport number that can be determined from the intercept and the slope of the linear plot of  $\ln(q_t/q_e)$  against  $\ln(t)$ . As shown in Table 5, the values of  $m$  were found to be less than 0.5 for adsorption of TPA and *p*-tol over the four adsorbents. The value of  $m$  is indicative of the type of transport mechanism. A value of  $m = 1$  would indicate the non-Fickian mechanism and  $m = 0.5$  represent the Fickian mechanism [75]. The constant  $k_m$  depends on the structural characteristics of adsorbent network in addition to its interaction with the adsorbates. The values of  $m < 0.5$  for the entire range of initial TPA and *p*-tol concentrations would indicate the Fickian diffusion of adsorbate molecules with surface interaction with each MOF.

### 3.3. Effect of pH on the adsorption of TPA and *p*-tol

The adsorption of organic compounds from aqueous solution is usually highly dependent on the pH of the solution [64]. The adsorption of TPA and *p*-tol was investigated at various pH values at a constant temperature of 25°C for a fixed adsorption time of 24 h. As shown in Fig. 8, the amounts of adsorbate adsorbed at equilibrium decreased with increasing pH of the solution. Generally, the chemical nature of the adsorbent surface which is influenced by the solution pH plays an important role in the adsorption of adsorbates from aqueous solutions [64]. The zeta potential of adsorbents in solutions also decreased with increasing pH (Fig. 5) indicating that the amount of the positive

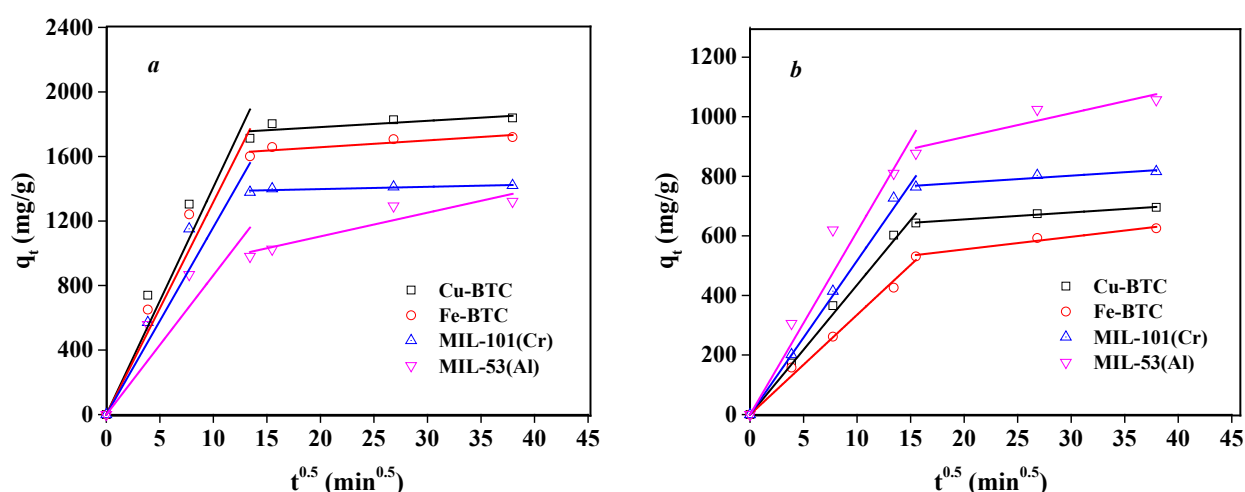


Fig. 7. Diffusion model plots for the adsorption of (a) TPA and (b) *p*-tol over different MOFs at  $T = 25^\circ\text{C}$  and initial concentration  $C_0 = 2000 \text{ mg/l}$ .

Table 5

Intraparticle diffusion constants and mode of diffusion parameters of TPA and *p*-tol over different MOFs at various initial concentrations

Adsorbate	Adsorbent	$C_o$ (mg/l)	Intraparticle diffusion rate		Mode of diffusion	
			$k_d$ (mg/g.min <sup>1/2</sup> )	$F$	$m$	$k_m$
TPA	Cu-BTC	1000	2.433	991.255	0.207	0.266
		2000	3.894	1704.155	0.194	0.290
	Fe-BTC	1000	3.256	936.015	0.217	0.249
		2000	4.230	1572.676	0.204	0.273
	MIL-101(Cr)	1000	2.177	707.04	0.191	0.296
		2000	1.416	1369.38	0.183	0.316
	MIL-53(Al)	1000	8.137	448.263	0.199	0.256
		2000	14.702	810.458	0.186	0.277
<i>p</i> -tol	Cu-BTC	1000	1.739	426.470	0.298	0.145
		2000	2.334	608.644	0.304	0.140
	Fe-BTC	1000	2.992	315.985	0.312	0.122
		2000	4.216	470.335	0.316	0.119
	MIL-101(Cr)	1000	1.248	523.938	0.301	0.144
		2000	2.320	732.605	0.310	0.136
	MIL-53(Al)	1000	5.109	530.484	0.261	0.176
		2000	8.013	771.635	0.265	0.172

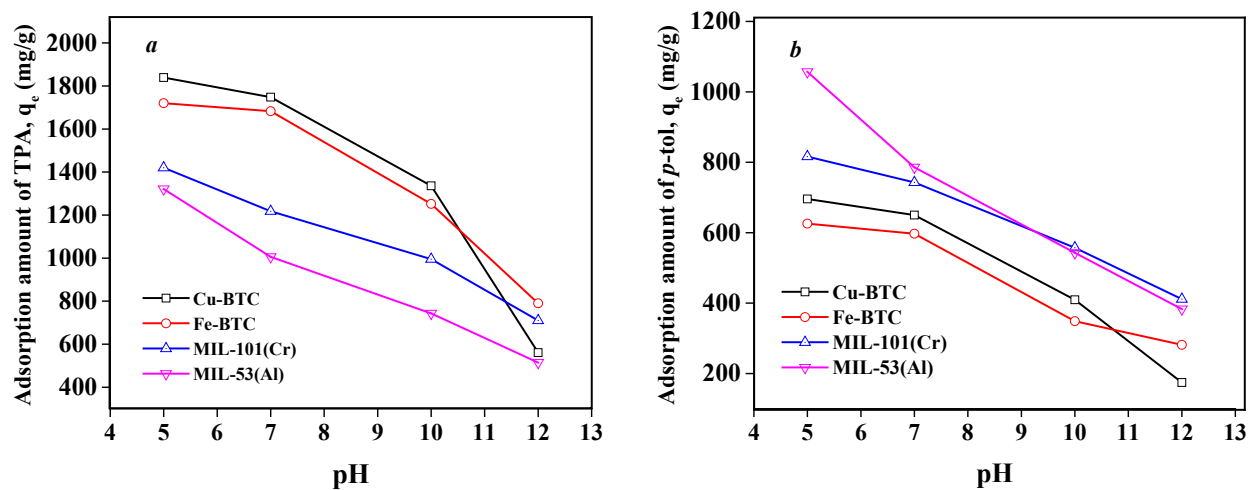


Fig. 8. Effect of solution pH on the adsorption of (a) TPA and (b) *p*-tol over four MOFs (initial concentration = 2000 mg/l and T = 25°C).

charges of the MOFs decreased with increasing pH values. Consequently, adsorption at higher pH led to a comparatively weaker interaction between TPA (or *p*-tol) anion and the surface of MOFs (less positive) which resulted in a decrease in adsorption capacity [79]. On the other hand, TPA and *p*-tol are weak acids with a  $pK_a$  value of 4.82 and 4.35 at 25°C, respectively. At a lower pH, the molecular form (acid-base interaction) is the predominant species and both TPA and *p*-tol have tendency for deposition and separation from water (resulting in error in calculations) while at a higher pH, due to deprotonation, the ionized form is the predominant species (the electrostatic interaction is more effective). Molecular and ionized forms may have different adsorption behaviors onto the adsorbent surface. The

solution pH affects both the surface charge of the adsorbent and the degree of ionization of the organic compound [12]. A lower adsorption at higher pH may be due to the abundance of OH<sup>-</sup> ions and consequent ionic repulsion between the negatively charged surface and the ionic organic compounds [55]. In this work, we chose pH = 5 as the optimum pH value for all experiments (to avoid errors in calculation, results for pH values below 5 were not considered). As shown in Fig. 8, at pH > 10, the adsorption amount of TPA and *p*-tol over Cu-BTC decreased drastically. This is due to the destruction of Cu-BTC structure at pH > 10 (the color of the solution containing Cu-BTC changed from light blue to dark gray) as also reported by other investigators report [80,81].

### 3.4. Adsorption experiments with a real wastewater

To compare the performance of the synthesized MOFs with two conventional adsorbents (activated carbon (AC) and multiwall carbon nanotubes (MWCNT)) using an industrial wastewater (WW), samples were obtained from the wastewater stream of the PTA (purified terephthalic acid) production plant in Mahshahr, Iran. The samples were taken from the WW stream of crude terephthalic acid (CTA) section (concentrated WW stream of catalyst recovery and washing sections to the water treatment unit). The characteristics of this stream is presented in Table 6 indicating that in addition of TPA and *p*-tol, there were significant quantities of other organic compounds including benzoic acid and the total solids (TS) that contained a variety of likely multi-cyclic organic compounds named high and low boiling byproducts. The wastewater adsorption experiments were performed with similar amounts of each adsorbent (0.1 g) in 20 ml of the WW. The WW containing the adsorbent was mixed well with magnetic stirring and maintained for 24 h at a constant temperature of 25°C. Subsequently, the solutions were separated from the adsorbents with a slow flow cellulose filter paper (2–3 μm) and the percentage of TPA (or *p*-tol) adsorption, *q*, and COD (chemical oxygen demand) removal from the WW were determined by the following equations:

$$q = \left( \frac{C_0 - C_e}{C_0} \right) \times 100(\%) \quad (12)$$

$$\text{COD} = \left( \frac{\text{COD}_0 - \text{COD}_e}{\text{COD}_0} \right) \times 100(\%) \quad (13)$$

where  $C_0$  and  $C_e$  (mg/l) are the initial and final concentration of TPA (or *p*-tol) in solution after 24 h, respectively, and  $\text{COD}_0$  and  $\text{COD}_e$  (mg/l) are the initial and final COD of WW after 24 h, respectively. According to Table 6, the concentration of TPA in this industrial WW is significantly higher than *p*-tol (almost 40 times). As shown in Fig. 9a, the removal of both TPA and *p*-tol over all MOFs were higher compared with AC and MWCNT as adsorbents. MIL-101(Cr) and MIL-53(Al) had a better performance than the other MOFs. Due to the presence of various organic compounds in the WW sample, the amounts of TPA and *p*-tol uptake from the industrial WW

Table 6  
Characteristics of the raw purified terephthalic acid wastewater samples used in this study

Stream	Item	Amount	Unit
PTA unit WW	pH	4.5	–
	Benzoic acid	1600	mg/l
	Terephthalic acid	2050	mg/l
	<i>p</i> -toluic acid	50	mg/l
	Total solid (after liquid vaporization of sample)	2.3	wt.%
	COD (chemical oxygen demand)	32900	mg/l

were lower than those for laboratory experiments with TPA (or *p*-tol) as the single adsorbate. For example, the TPA uptake of MIL-53(Al) from WW was 261.1 mg/g, while for an aqueous laboratory solution of TPA with the same initial concentration, the amount of TPA adsorbed over the MIL-53(Al) was 1321.4 mg/g. The simultaneous adsorption of other cyclic pollutants in addition to TPA and *p*-tol resulted in COD reduction of 9500, 7800, 10400 and 9400 mg/l for industrial WW when Cu-BTC, Fe-BTC, MIL-53(Al) and MIL-101(Cr) were used as adsorbent, respectively. The COD of a laboratory solution of TPA and *p*-tol with the same concentration as the WW stream was ~3100 mg/l that is much lower than COD removed by adsorbents from WW stream. Fig. 9b shows the %COD removal of WW using different adsorbents indicating the superiority of MOFs, especially mesoporous MIL-53(Al), as the promising adsorbents for wastewater treatment processes. Comparison between the results from this work and the results presented by other investigators presented in Table 7 confirms the versatility of MOFs in removal of TPA or *p*-tol from water.

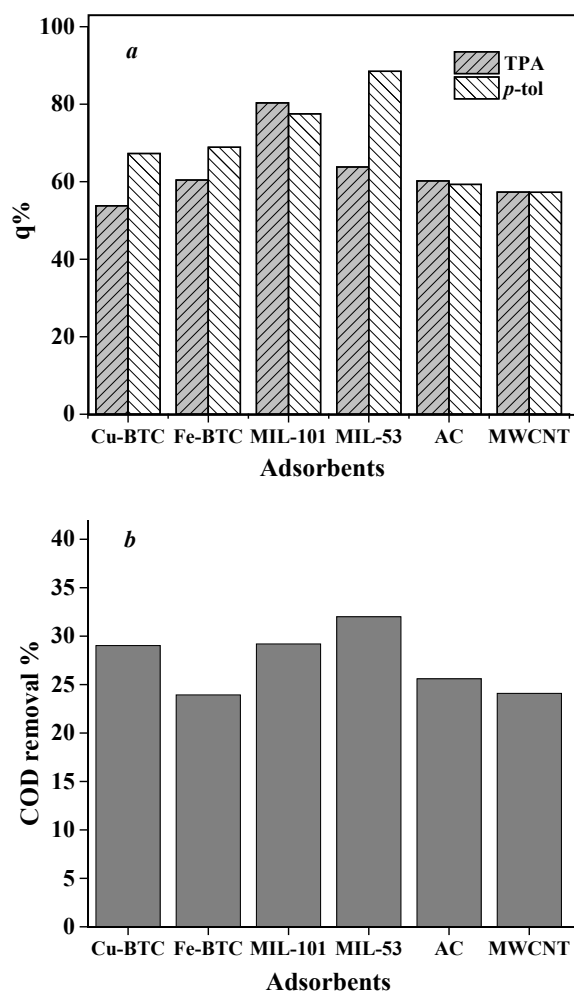


Fig. 9. (a) Percentage of TPA and *p*-tol adsorption (*q*%) over different adsorbents in the selected industrial WW, (b) percentage of COD removed from WW samples.

Table 7  
Comparison between adsorption results of this work with other investigations

Adsorbent	Adsorbate	$q_{e,exp}$	Reference
TiO <sub>2</sub>	TPA	27mg/g	[6]
CMK-1/PDDA	TPA, <i>p</i> -tol	143, 90 mg/g	[3]
Microbial fuel cell (MFC)	TPA, <i>p</i> -tol	100, 42 mg/l·day	[5]
Ferric chloride	TPA	650 mg/g	[82]
Diatomite	TPA	5 mg/g	[83]
Multiwall carbon nanotubes	TPA, <i>p</i> -tol	975.7, 597.2 mg/g	This work
Activated carbon	TPA, <i>p</i> -tol	1117.2, 632.9 mg/g	This work
Cu-BTC	TPA, <i>p</i> -tol	1838.6, 695.7 mg/g	This work
Fe-BTC	TPA, <i>p</i> -tol	1720, 625.7 mg/g	This work
MIL-101(Cr)	TPA, <i>p</i> -tol	1420.1, 816.3 mg/g	This work
MIL-53(Al)	TPA, <i>p</i> -tol	1321.4, 1056.7 mg/g	This work

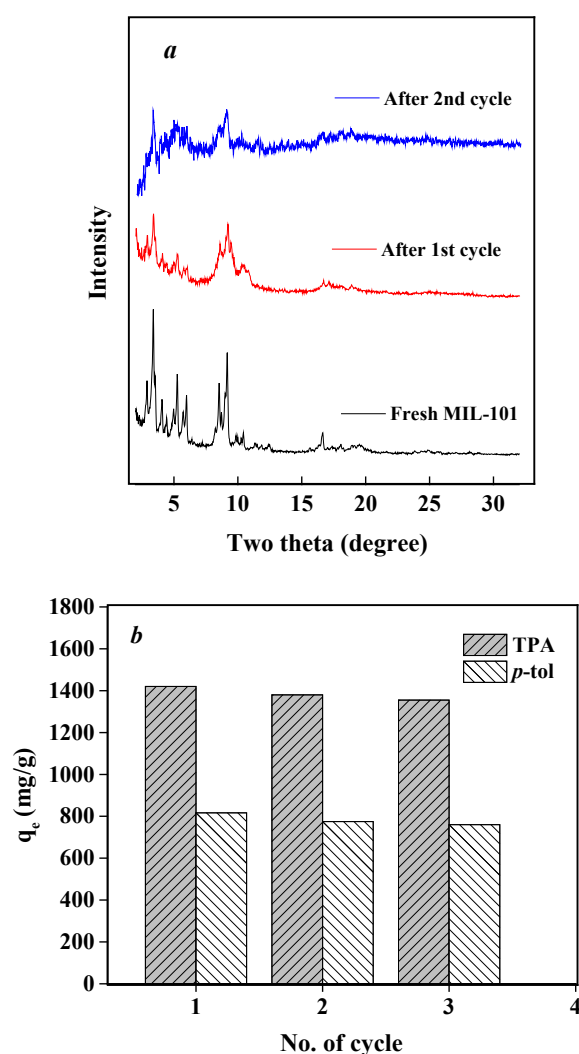


Fig. 10. Reusability of MIL-101 for adsorption of TPA and *p*-tol: (a) comparison of XRD patterns of fresh and reused MIL-101 and (b) effect of the number of recycles on the equilibrium adsorption capacity.

### 3.5. Reusability

The reusability of adsorbents was evaluated after washing the used MOFs with dried ethanol and water. After regeneration with solvent wash, the crystal structure of the MOFs was retained. For example, in XRD patterns of MIL-101(Cr) after two times recycling, the main intensities at  $2\theta = 2.5$  to 10 degrees were retained (Fig. 10a). Even though the adsorbed amounts decreased slightly with the number of recycles, the adsorbed amounts did not change remarkably after two regeneration cycles (Fig. 10b). In addition, the trace amounts (<0.1~0.2 ppm) of Cr, Al, Fe and Cu in filtrate from ICP analysis (due to decomposition of Cu-BTC at pH > 10, the amount of Cu in filtrate was significant for these pH value) confirm the stability of MOFs in aqueous media and their potential in commercial applications.

### 4. Conclusions

The liquid-phase adsorption of TPA and *p*-tol using four well-known MOFs including Cu-BTC, Fe-BTC, MIL-101(Cr), and MIL-53(Al) was reported for the first time and compared with two conventional adsorbents AC and MWCNT. The equilibrium adsorption isotherms were adequately described by the Langmuir and Redlich-Peterson models. The dynamic adsorption data was well-fitted with a pseudo-second order kinetic model. For each MOF, the adsorption capacity was higher for TPA compared with *p*-tol. The highest adsorption capacity for TPA was obtained with Cu-BTC (~1840 mg/g). This could be due to (a) favorable physicochemical properties including polarizability, polar surface area, electron affinity, and the length of the diagonal plane of TPA compared with *p*-tol, and (b) the characteristic of Cu-BTC structure having small pore diameter and high ratio of micropore volume resulting in an increase in the adsorbate-adsorbent and intermolecular interactions (micropore filling). For *p*-tol, the highest adsorption capacity was obtained with MIL-53(Al) (~1060 mg/g) which could be due to (a) the polarity (dipole moment) and lower surface tension of *p*-tol and (b) breathing effect, the higher positive surface charge, and

the higher mesopore volume of MIL-53(Al) resulting in an increase in the dispersive and capillary forces in MIL-53(Al) as compared with other adsorbents for adsorption of polar organic components such as *p*-tol. The lower solution pH, (of about 5) was found to be more favorable for the adsorption of the TPA and *p*-tol over four MOFs indicating the importance of simple electrostatic interaction between the organic adsorbates and adsorbents for the adsorption process. Adsorption studies involving an industrial wastewater stream of a purified TPA production plant and the reusability of MOFs by simply washing the spent solids with ethanol and water suggested that, compared with conventional adsorbents such as AC and MWCNT, MOFs (especially mesopore-types) can be used as promising adsorbents in the adsorptive removal of organic pollutants from contaminated waters.

### Acknowledgements

The financial support by Shahid Tondgooyan Petrochemical Company (STPC) is gratefully acknowledged.

### References

- [1] A. Shafaei, M. Nikazar, M. Arami, Photocatalytic degradation of terephthalic acid using titania and zinc oxide photocatalysts: Comparative study, *Desalination*, 252 (2010) 8–16.
- [2] M. Davarpanah, A. Ahmadpour, T.R. Bastami, Preparation and characterization of anion exchange resin decorated with magnetite nanoparticles for removal of *p*-toluic acid from aqueous solution, *J. Magn. Magn. Mater.*, 375 (2015) 177–183.
- [3] M. Anbia, S. Salehi, Synthesis of polyelectrolyte-modified ordered nanoporous carbon for removal of aromatic organic acids from purified terephthalic acid wastewater, *Chem. Eng. Res. Des.*, 90 (2012) 975–983.
- [4] J.Y. Joung, H.W. Lee, H. Choi, M.W. Lee, J.M. Park, Influences of organic loading disturbances on the performance of anaerobic filter process to treat purified terephthalic acid wastewater, *Bioresour. Technol.*, 100 (2009) 2457–2461.
- [5] S.K.F. Marashi, H.-R. Kariminia, I.S.P. Savizi, Bimodal electricity generation and aromatic compounds removal from purified terephthalic acid plant wastewater in a microbial fuel cell, *Biotechnol. Lett.*, 35 (2013) 197–203.
- [6] O. Caliskan, A.D. Ilgun, M. Yilmaz, H.B. Yener, S.F. Ozkan, S.S. Helvacı, Adsorption behavior of terephthalic acid on TiO<sub>2</sub> nano particles synthesized by thermal hydrolysis method, *J. Selcuk Univ. Natural and Applied Science*, 28 (2013) 828–834.
- [7] P. Khachane, A. Heesink, G. Versteeg, V. Pangarkar, Adsorptive separation and recovery of organic compounds from purified terephthalic acid plant effluent, *Separ. Sci. Technol.*, 38 (2003) 93–111.
- [8] E. Ayranci, N. Hoda, E. Bayram, Adsorption of benzoic acid onto high specific area activated carbon cloth, *J. Colloid Interf. Sci.*, 284 (2005) 83–88.
- [9] J.M. Chern, Y.W. Chien, Competitive adsorption of benzoic acid and *p*-nitrophenol onto activated carbon: isotherm and breakthrough curves, *Water Res.*, 37 (2003) 2347–2356.
- [10] L. Huang, H. Xiao, Y. Ni, Cationic MCM-41: synthesis, characterization and sorption behavior towards aromatic compounds, *Colloid. Surface. A*, 247 (2004) 129–136.
- [11] R. Kleerebezem, L.W.H. Pol, G. Lettinga, Anaerobic biodegradability of phthalic acid isomers and related compounds, *Bio-degradation*, 10 (1999) 63–73.
- [12] N. Yıldız, R. Gönülşen, H. Koyuncu, A. Çalmlı, Adsorption of benzoic acid and hydroquinone by organically modified bentonites, *Colloid. Surface. A*, 260 (2005) 87–94.
- [13] R.J. Kuppler, D.J. Timmons, Q.-R. Fang, J.-R. Li, T.A. Makal, M.D. Young, D. Yuan, D. Zhao, W. Zhuang, H.-C. Zhou, Potential applications of metal-organic frameworks, *Coordin. Chem. Rev.*, 253 (2009) 3042–3066.
- [14] S.H. Jhung, N.A. Khan, Z. Hasan, Analogous porous metal-organic frameworks: synthesis, stability and application in adsorption, *Cryst. Eng. Comm.*, 14 (2012) 7099–7109.
- [15] B. Van de Voorde, B. Bueken, J. Denayer, D. De Vos, Adsorptive separation on metal-organic frameworks in the liquid phase, *Chem. Soc. Rev.*, 43 (2014) 5766–5788.
- [16] L. Hamon, C. Serre, T. Devic, T. Loiseau, F. Millange, G. Férey, G.D. Weireld, Comparative study of hydrogen sulfide adsorption in the MIL-53 (Al, Cr, Fe), MIL-47 (V), MIL-100 (Cr), and MIL-101 (Cr) metal-organic frameworks at room temperature, *J. Am. Chem. Soc.*, 131 (2009) 8775–8777.
- [17] J. R. Li, R.J. Kuppler, H.C. Zhou, Selective gas adsorption and separation in metal-organic frameworks, *Chem. Soc. Rev.*, 38 (2009) 1477–1504.
- [18] J. Lee, O.K. Farha, J. Roberts, K.A. Scheidt, S.T. Nguyen, J.T. Hupp, Metal-organic framework materials as catalysts, *Chem. Soc. Rev.*, 38 (2009) 1450–1459.
- [19] D. Farrusseng, S. Aguado, C. Pinel, Metal-organic frameworks: opportunities for catalysis, *Angew. Chem. Int. Edit.*, 48 (2009) 7502–7513.
- [20] M. Allendorf, C. Bauer, R. Bhakta, R. Houk, Luminescent metal-organic frameworks, *Chem. Soc. Rev.*, 38 (2009) 1330–1352.
- [21] Y. Cui, Y. Yue, G. Qian, B. Chen, Luminescent functional metal-organic frameworks, *Chem. Rev.*, 112 (2011) 1126–1162.
- [22] P. Horcajada, C. Serre, M. Vallet-Regí, M. Sebba, F. Taulelle, G. Férey, Metal-organic frameworks as efficient materials for drug delivery, *Angew. Chem. Ger. Edit.*, 118 (2006) 6120–6124.
- [23] Q.M. Wang, D. Shen, M. Bülow, M.L. Lau, S. Deng, F.R. Fitch, N.O. Lemcoff, J. Semanscin, Metallo-organic molecular sieve for gas separation and purification, *Micropor. Mesopor. Mat.*, 55 (2002) 217–230.
- [24] J.W. Yoon, Y.K. Seo, Y.K. Hwang, J.S. Chang, H. Leclerc, S. Wutke, P. Bazin, A. Vimont, M. Daturi, E. Bloch, Controlled reducibility of a metal-organic framework with coordinatively unsaturated sites for preferential gas sorption, *Angew. Chem. Int. Edit.*, 49 (2010) 5949–5952.
- [25] O. Lebedev, F. Millange, C. Serre, G. Van Tendeloo, G. Férey, First direct imaging of giant pores of the metal-organic framework MIL-101, *Chem. Mater.*, 17 (2005) 6525–6527.
- [26] J. Yang, Q. Zhao, J. Li, J. Dong, Synthesis of metal-organic framework MIL-101 in TMAOH-Cr (NO<sub>3</sub>)<sub>3</sub>-H<sub>2</sub>O and its hydrogen-storage behavior, *Micropor. Mesopor. Mat.*, 130 (2010) 174–179.
- [27] P. Rallapalli, D. Patil, K. Prasanth, R.S. Somani, R. Jasra, H. Bajaj, An alternative activation method for the enhancement of methane storage capacity of nanoporous aluminium terephthalate, MIL-53 (Al), *J. Porous Mat.*, 17 (2010) 523–528.
- [28] D.V. Patil, P.B.S. Rallapalli, G.P. Dangi, R.J. Tayade, R.S. Somani, H.C. Bajaj, MIL-53 (Al): an efficient adsorbent for the removal of nitrobenzene from aqueous solutions, *Ind. Eng. Chem. Res.*, 50 (2011) 10516–10524.
- [29] A. Vishnyakov, P.I. Ravikovitch, A.V. Neimark, M. Bülow, Q.M. Wang, Nanopore structure and sorption properties of Cu-BTC metal-organic framework, *Nano Lett.*, 3 (2003) 713–718.
- [30] G.W. Peterson, G.W. Wagner, A. Balboa, J. Mahle, T. Sewell, C.J. Karwacki, Ammonia vapor removal by Cu<sub>3</sub>(BTC)<sub>2</sub> and its characterization by MAS NMR, *J. Phys. Chem. C*, 113 (2009) 13906–13917.
- [31] F. Tan, M. Liu, K. Li, Y. Wang, J. Wang, X. Guo, G. Zhang, C. Song, Facile synthesis of size-controlled MIL-100 (Fe) with excellent adsorption capacity for methylene blue, *Chem. Eng. J.*, 281 (2015) 360–367.
- [32] S. H. Huo, X.P. Yan, Metal-organic framework MIL-100 (Fe) for the adsorption of malachite green from aqueous solution, *J. Mater. Chem.*, 22 (2012) 7449–7455.
- [33] Z. Zhao, X. Li, Z. Li, Adsorption equilibrium and kinetics of *p*-xylene on chromium-based metal organic framework MIL-101, *Chem. Eng. J.*, 173 (2011) 150–157.

- [34] C.X. Yang, S.S. Liu, H.F. Wang, S.W. Wang, X.P. Yan, High-performance liquid chromatographic separation of position isomers using metal–organic framework MIL-53 (Al) as the stationary phase, *Analyst*, 137 (2012) 133–139.
- [35] M. Opanasenko, A. Dhakshinamoorthy, M. Shamzhy, P. Nachtigall, M. Horáček, H. Garcia, J. Čejka, Comparison of the catalytic activity of MOFs and zeolites in Knoevenagel condensation, *Cat. Sci. Tec.*, 3 (2013) 500–507.
- [36] J. Shi, S. Hei, H. Liu, Y. Fu, F. Zhang, Y. Zhong, W. Zhu, Synthesis of MIL-100 (Fe) at low temperature and atmospheric pressure, *J. Chem.*, 2013 (2013) 1–4.
- [37] C. Li, Z. Xiong, J. Zhang, C. Wu, The Strengthening Role of the Amino Group in Metal–Organic Framework MIL-53 (Al) for Methylene Blue and Malachite Green Dye Adsorption, *J. Chem. Eng. Data*, 60 (2015) 3414–3422.
- [38] K. Yang, Q. Sun, F. Xue, D. Lin, Adsorption of volatile organic compounds by metal–organic frameworks MIL-101: Influence of molecular size and shape, *J. Hazard. Mater.*, 195 (2011) 124–131.
- [39] Y. Li, R.T. Yang, Hydrogen storage in metal–organic and covalent–organic frameworks by spillover, *AIChE J.*, 54 (2008) 269–279.
- [40] H. Hosseini-Monfared, C. Näther, H. Winkler, C. Janiak, Highly selective and “green” alcohol oxidations in water using aqueous 10% H<sub>2</sub>O<sub>2</sub> and iron-benzenetricarboxylate metal–organic gel, *Inorg. Chim. Acta*, 391 (2012) 75–82.
- [41] P. Chowdhury, C. Bikkina, D. Meister, F. Dreisbach, S. Gumma, Comparison of adsorption isotherms on Cu-BTC metal organic frameworks synthesized from different routes, *Micropor. Mesopor. Mat.*, 117 (2009) 406–413.
- [42] D. Zacher, R. Schmid, C. Wöll, R.A. Fischer, Surface chemistry of metal–organic frameworks at the liquid–solid interface, *Angew. Chem. Int. Edit.*, 50 (2011) 176–199.
- [43] S.H. Huo, X.P. Yan, Facile magnetization of metal–organic framework MIL-101 for magnetic solid-phase extraction of polycyclic aromatic hydrocarbons in environmental water samples, *Analyst*, 137 (2012) 3445–3451.
- [44] S. Li, F. Huo, Metal–organic framework composites: from fundamentals to applications, *Nanoscale*, 7 (2015) 7482–7501.
- [45] Z. Hasan, E.J. Choi, S.H. Jhung, Adsorption of naproxen and clofibric acid over a metal–organic framework MIL-101 functionalized with acidic and basic groups, *Chem. Eng. J.*, 219 (2013) 537–544.
- [46] L. Zhu, H. Yu, H. Zhang, J. Shen, L. Xue, C. Gao, B. van der Bruggen, Mixed matrix membranes containing MIL-53 (Al) for potential application in organic solvent nanofiltration, *RSC Adv.*, 5 (2015) 73068–73076.
- [47] K. Foo, B. Hameed, Insights into the modeling of adsorption isotherm systems, *Chem. Eng. J.*, 156 (2010) 2–10.
- [48] H. Zheng, D. Liu, Y. Zheng, S. Liang, Z. Liu, Sorption isotherm and kinetic modeling of aniline on Cr-bentonite, *J. Hazard. Mater.*, 167 (2009) 141–147.
- [49] S. Giraudet, P. Pré, H. Tezel, P. Le Cloirec, Estimation of adsorption energies using physical characteristics of activated carbons and VOCs’ molecular properties, *Carbon*, 44 (2006) 1873–1883.
- [50] G.Q. Guo, H. Chen, Y.C. Long, Separation of *p*-xylene from C 8 aromatics on binder-free hydrophobic adsorbent of MFI zeolite. I. Studies on static equilibrium, *Micropor. Mesopor. Mat.*, 39 (2000) 149–161.
- [51] C. Herry, M. Baudu, D. Raveau, Estimation of the influence of structural elements of activated carbons on the energetic components of adsorption, *Carbon*, 39 (2001) 1879–1889.
- [52] P. Reucroft, D. Rivin, Gas/vapor flow microcalorimetry on porous carbons II. Heat of adsorption of toluene on microporous/mesoporous carbons, *Thermochim. Acta*, 328 (1999) 19–24.
- [53] R. Bradley, B. Rand, On the physical adsorption of vapors by microporous carbons, *J. Colloid Interf. Sci.*, 169 (1995) 168–176.
- [54] W. Zhang, Z. Xu, B. Pan, C. Hong, K. Jia, P. Jiang, Q. Zhang, B. Pan, Equilibrium and heat of adsorption of diethyl phthalate on heterogeneous adsorbents, *J. Colloid Interf. Sci.*, 325 (2008) 41–47.
- [55] N.A. Khan, B.K. Jung, Z. Hasan, S.H. Jhung, Adsorption and removal of phthalic acid and diethyl phthalate from water with zeolitic imidazolate and metal–organic frameworks, *J. Hazard. Mater.*, 282 (2015) 194–200.
- [56] I. Basheer, Y. Najjar, M. Hajmeer, Neuronet modeling of VOC adsorption by GAC, *Environ. Technol.*, 17 (1996) 795–806.
- [57] P. Pré, F. Delage, C. Faur-Brasquet, P. Le Cloirec, Quantitative structure–activity relationships for the prediction of VOCs adsorption and desorption energies onto activated carbon, *Fuel Process. Technol.*, 77 (2002) 345–351.
- [58] V. Ponec, Z. Knor, Černý S. Adsorption on solids, English translation, London: Butterworth, (1974).
- [59] J. Rouquerol, F. Rouquerol, P. Llewellyn, G. Maurin, K.S. Sing, Adsorption by powders and porous solids: principles, methodology and applications, Academic press, 2013.
- [60] M. Tuller, D. Or, L.M. Dudley, Adsorption and capillary condensation in porous media: Liquid retention and interfacial configurations in angular pores, *Water Resour. Res.*, 35 (1999) 1949–1964.
- [61] E. Haque, N.A. Khan, S.N. Talapaneni, A. Vinu, J.-G. JeGal, S.-H. Jhung, Adsorption of phenol on mesoporous carbon CMK-3: effect of textural properties, *B. Kor. Chem. Soc.*, 31 (2010) 1638–1642.
- [62] H. Cherifi, S. Hanini, F. Bentahar, Adsorption of phenol from wastewater using vegetal cords as a new adsorbent, *Desalination*, 244 (2009) 177–187.
- [63] Z. Hasan, J. Jeon, S.H. Jhung, Adsorptive removal of naproxen and clofibric acid from water using metal–organic frameworks, *J. Hazard. Mater.*, 209 (2012) 151–157.
- [64] A. Mestre, M. Pinto, J. Pires, J. Nogueira, A. Carvalho, Effect of solution pH on the removal of clofibric acid by cork-based activated carbons, *Carbon*, 48 (2010) 972–980.
- [65] A. Dada, A. Olalekan, A. Olatunya, O. Dada, Langmuir, Freundlich, Temkin and Dubinin–Radushkevich isotherms studies of equilibrium sorption of Zn<sup>2+</sup> onto phosphoric acid modified rice husk, *J. Appl. Chem.*, 3 (2012) 38–45.
- [66] C. Chen, M. Zhang, Q. Guan, W. Li, Kinetic and thermodynamic studies on the adsorption of xylene orange onto MIL-101 (Cr), *Chem. Eng. J.*, 183 (2012) 60–67.
- [67] F.C. Wu, B.L. Liu, K.T. Wu, R.L. Tseng, A new linear form analysis of Redlich–Peterson isotherm equation for the adsorptions of dyes, *Chem. Eng. J.*, 162 (2010) 21–27.
- [68] M. Ahmaruzzaman, D. Sharma, Adsorption of phenols from wastewater, *J. Colloid Interf. Sci.*, 287 (2005) 14–24.
- [69] J. Wu, L.G. Hammarstrom, O. Claesson, I. Fangmark, Modeling the influence of physico-chemical properties of volatile organic compounds on activated carbon adsorption capacity, *Carbon*, 41 (2003) 1322–1325.
- [70] N.A. Khan, S.H. Jhung, Remarkable Adsorption Capacity of CuCl<sub>2</sub>-Loaded Porous Vanadium Benzenedicarboxylate for Benzothiophene, *Angew. Chem. Ger. Edit.*, 124 (2012) 1224–1227.
- [71] L. Hamon, H. Leclerc, A. Ghoufi, L. Oliviero, A. Travert, J.-C. Lavalley, T. Devic, C. Serre, G. Férey, G. De Weireld, Molecular insight into the adsorption of H<sub>2</sub>S in the flexible MIL-53 (Cr) and rigid MIL-47 (V) MOFs: infrared spectroscopy combined to molecular simulations, *J. Phys. Chem. C*, 115 (2011) 2047–2056.
- [72] D.L. Guerra, C. Airolidi, V.P. Lemos, R.S. Angelica, Adsorptive, thermodynamic and kinetic performances of Al/Ti and Al/Zr-pillared clays from the Brazilian Amazon region for zinc cation removal, *J. Hazard. Mater.*, 155 (2008) 230–242.
- [73] E. Haque, N.A. Khan, J.H. Park, S.H. Jhung, Synthesis of a metal–organic framework material, iron terephthalate, by ultrasound, microwave, and conventional electric heating: a kinetic study, *Chem. Eur. J.*, 16 (2010) 1046–1052.
- [74] F. Leng, W. Wang, X.J. Zhao, X.L. Hu, Y.F. Li, Adsorption interaction between a metal–organic framework of chromium–benzenedicarboxylates and uranine in aqueous solution, *Colloid. Surface. A*, 441 (2014) 164–169.
- [75] T.W. Weber, R.K. Chakravorti, Pore and solid diffusion models for fixed-bed adsorbents, *AIChE J.*, 20 (1974) 228–238.

- [76] R. Arasteh, M. Masoumi, A. Rashidi, L. Moradi, V. Samimi, S. Mostafavi, Adsorption of 2-nitrophenol by multi-wall carbon nanotubes from aqueous solutions, *Appl. Surf. Sci.*, 256 (2010) 4447–4455.
- [77] C.B. Vidal, A.L. Barros, C.P. Moura, A.C. De Lima, F.S. Dias, L.C. Vasconcelos, P.B. Fecine, R.F. Nascimento, Adsorption of polycyclic aromatic hydrocarbons from aqueous solutions by modified periodic mesoporous organosilica, *J. Colloid Interf. Sci.*, 357 (2011) 466–473.
- [78] L. Xie, D. Liu, H. Huang, Q. Yang, C. Zhong, Efficient capture of nitrobenzene from waste water using metal–organic frameworks, *Chem. Eng. J.*, 246 (2014) 142–149.
- [79] H. Oda, M. Kishida, C. Yokokawa, Adsorption of benzoic acid and phenol from aqueous solution by activated carbons—effect of surface acidity, *Carbon*, 19 (1981) 243–248.
- [80] S. Lin, Z. Song, G. Che, A. Ren, P. Li, C. Liu, J. Zhang, Adsorption behavior of metal–organic frameworks for methylene blue from aqueous solution, *Micropor. Mesopor. Mat.*, 193 (2014) 27–34.
- [81] S. Marx, W. Kleist, A. Baiker, Synthesis, structural properties, and catalytic behavior of Cu-BTC and mixed-linker Cu-BTC-PyDC in the oxidation of benzene derivatives, *J. Catal.*, 281 (2011) 76–87.
- [82] Y.Z. Wen, S.P. Tong, K.F. Zheng, L.L. Wang, J.Z. Lv, J. Lin, Removal of terephthalic acid in alkalized wastewater by ferric chloride, *J. Hazard. Mater.*, 138 (2006) 169–172.
- [83] W.S. Linghu, R.P. Shen, Removal of terephthalic acid from waste Water using diatomite adsorbent, *Mater. Sci. Forum*, 787 (2014) 82–91.